Supporting Information for "The Earth surface controls the depth-dependent seismic radiation of megathrust earthquakes"

Jiuxun Yin[1], Marine A. Denolle[1,2]

[1]Department of Earth and Planetary Sciences, Harvard University

[2]Department of Earth and Space Sciences, University of Washington

Contents of this file

1. Text S1 to S4

2. Figures S1 to S5

3. Table S1

Additional Supporting Information (Files uploaded separately) Caption of the figures. Each figure contains 8 subfigures to show model settings and results. (a) The structure of model: topography, fault geometry, P wave velocity. The blue outlined region (if any) indicates the region where we set the Vp/Vs ratio to the given value. (b) Initial stress distributions along depth (black line: initial shear stress τ_0; gray line: initial effective normal stress $\bar{\sigma}_0$. (c) Parameters of used friction law along depth: upper X-axis shows the friction coefficients (red dashed line: dynamic friction coefficient μ_d; red solid line: static friction coefficient μ_s), bottom X-axis shows the critical slip D_c in black line. (d) Space-time evolution of the rupture (in blue image) and of selected points on the fault (black lines), including the one at the trench/surface (thick black line). Gray and red lines show the updip- and downdip-propagating rupture front, respectively. We estimate

February 10, 2021, 5:06pm

21 the rupture velocity by linear fitting the location and time of rupture front. (e) Slip-rate

22 functions along fault segments, aligned to their onset time (when rupture front arrives).

23 The location of the fault segment center taken as the alongdip distance from the trench is

24 indicated by the gray colormap. (f) Normalized Fourier amplitude spectra corresponding

25 to the slip-rate functions shown in (e). The same color scheme is used to indicate the

26 fault segment location. (g) moment-rate density function averaged along the entire fault.

27 (h) The along-dip best-fit spectral parameters of the spectra in (f) as well as its 95%

28 confidence interval. The right Y-axis shows the corner frequency f_c in red. The left

29 Y-axis shows the spectral falloff rate n in blue.

Introduction

In this Supporting Information, we show all the detailed information about our dynamic rupture models. The model setup details include model setting, friction, initial stress, and software information. All simulation settings and results of each model are included in Supporting Information 2, which is a Zip file of Figures including the model parameters ((a) structures, (b) stress, (c) friction), simulations results ((d) - (g)) and the fitting of spectral parameters ((h) corner frequency f_c and spectral falloff rate n).

1. Text S1. Model setting

The entire simulation with free surface is in a semicircle domain with a radius of 350 km and centered at X = 150 km, Y = 0 km. The simulation domain consists of 1) a near-source and detailed rectangular structure of dimension 270 km × 50 km (black box area in Fig. S2a), and 2) a far-source homogeneous half-space (Fig. S2).

In the near-source region, we test different structural settings: Planar fault embedded in the homogeneous velocity structure and flat topography (Model 1 and Model 15); Curved fault embedded in the homogeneous velocity structure and flat topography (Model 2 and Model 16); Curved fault embedded in the homogeneous velocity structure and realistic topography (Model 3 and Model 17). The rest of the models use a curved fault embedded in heterogeneous velocity structure and realistic topography. We use the P-wave velocity model directly from Miura et al. (2005). We use the empirical relation of Brocher (2005) to calculate density from the V_P values, $\rho = 1.74(V_P)^{0.25}$. The S-wave velocity V_S is calculated from a V_P/V_S ratio structure. For most of the simulation domain, we fix the V_P/V_S ratio constant of $\sqrt{3} \approx 1.73$, assuming a Poisson medium. For specific regions detailed as the blue outlined region in Fig. 1b (also see Figure S1), we raise the V_P/V_S ratio to the following values: 1.83 (Models 8 and 22), 1.94 (Models 9 and 23) , 2.04

54 (Models 10 and 24), 2.14 (Models 11 and 25), 2.24 (Models 12 and 26), 2.34 (Models 13

55 and 27) and 2.45 (Models 14 and 28). For other heterogeneous models, the V_P/V_S ratio

56 is fixed constant $\sqrt{3} \approx 1.73$ (Models 4-7 and Models 18-21). Finally, we can get the shear

57 modulus $\mu = \rho V_S^2$.

58   For the homogeneous models in the far-source region, we have $V_P = 6.93$ km/s and

59 $V_S = 4$ km/s, which are the same as those in the near-source region of Models 1-3 and

60 15-17. For the heterogeneous models, $V_P = 8.30$ km/s is chosen as the maximum P wave

61 velocity in the model of Miura et al. (2005) and $V_S = 4.79$ km/s, corresponding to V_P/V_S

62 ratio $= \sqrt{3}$. To avoid strong wave reflections from steep velocity changes between the two

63 simulation domains, we set a 5-km wide transition zone with a smooth gradient in the

64 velocity values from the near-source to the far-source regions. At the boundaries of the

65 simulation domain, we set the traction-free boundary condition on the top surface (blue

66 line in Fig. S2), and the absorbing boundary condition (red line in Fig. S2) along the

67 borders of the semicircle domain.

2.   Text S2. Friction

68   For most of our simulations (all Models 4-6 and 18-20), we use the linear slip weakening

69 friction. The parameters of linear slip weakening are chosen constant from the surface

70 down to 40 km depth (Supporting Information 2 (b)): static friction coefficient $\mu_s = 0.677$;

71 dynamic friction coefficient $\mu_d = 0.2$; the critical slip of slip weakening $D_c = 0.4$ m. Below

72 40 km, we increase the dynamic friction coefficient to 0.99 to force the termination of the

73 rupture. While the focus of this study is not to explore all frictional relations, we test

74 several different friction relations above 10.8 km depth (at the base of the frontal prism)

75 to be slip neutral/stable ($\mu_s = \mu_d = 0.677$ above 10.8 km depth, Models 4 and 18) or

76 slip hardening/strengthening ($\mu_s = 0.677$, $\mu_s < \mu_d = 0.85$ and $D_c = 2$ m above 10.8 km

77 depth, Models 5 and 19). Finally, we include a model with the same lab-based exponential

78   slip weakening proposed by Murphy et al. (2018) in Models 6 and 20. We use the same

79   relations (See their equations (1) and (2)) to set up the stress and frictional parameters.

3.   Text S3. Initial stress

80   In our simulations, the effective normal stress $\bar{\sigma}_n$ is reduced from the fault normal stress

81   σ_L due to pore pressure p, $\bar{\sigma}_n = \sigma_L - p$. Because of the relatively low dip angle of the fault,

82   we approximate the normal stress σ_L as the lithostatic stress that is calculated based on

83   the density structure $\rho(x, h)$ of each model: $\sigma_L(x) = \int_{h_{slab}}^{h_0} \rho(x, h) g dh$, where h_{slab} and h_0

84   are the depths of slab surface and top free surface, g is the gravitation constant. We use

85   the fluid pressure ratio λ to quantify the pore pressure: $p = \lambda \sigma_L$. This quantification is

86   introduced by Hubbert and Rubey (1959) and has been used in many previous studies

87   (e.g., Murphy et al., 2018; Lotto et al., 2018). Finally, we assume the effective normal

88   stress $\bar{\sigma}_n$ is bounded at 40 MPa, at which the over-pressurized pore pressure becomes

89   lithostatic (Rice, 1992), corresponding to the case of $\lambda = 1.0$ (similar to the settings in

90   Lotto et al., 2018). In this study, we mainly vary λ for the stress setting variations of

91   models, and include cases of $\lambda = 0.9$ and $\lambda = 0.7$. This parameter controls how pore

92   pressure varies along depth and where the pore fluid becomes lithostatic (see Fig. 1c in

93   the main text).

We assume a relatively low initial shear stress τ_0 on the fault, and calculate it using the

seismic S ratio (Fig. 1c), which is used to measure how close the initial stress is to the

level of failure (Day, 1982):

$$S = \frac{\tau_s - \tau_0}{\tau_0 - \tau_d} = 2.77, \tag{1}$$

94   where $\tau_s = \bar{\sigma}_n \mu_s$ and $\tau_d = \bar{\sigma}_n \mu_d$ are the static friction (yielding stress) and dynamic fric-

95   tion, respectively. This high seismic S ratio is set to avoid the unwanted supershear rupture

96   that arises from high initial stress and resulting high dynamic stress drop (Andrews, 1985;

97 Dunham, 2007). Finally, we use over-stress nucleation to start the spontaneous dynamic

98 rupture for all models. We increase the initial shear stress to $1.016\tau_s$ within a 2-km patch

99 on fault centered at the depth of 20 km (Fig. 1c). The only exceptions are the models

100 with exponential slip weakening friction (Models 6 and 20) for which we have to set a

101 larger nucleation zone of about 14 km to successfully nucleate megathrust rupture. We

102 have checked the results of those models (Models 6 and 20) and can assure that this large

103 nucleation patch has negligible effects on the later dynamic rupture process.

4.   Text S4. Numerical solver

104 The entire domain is discretized with unstructured mesh using software CUBIT

105 (`https://cubit.sandia.gov/`, the mesh script is written based on Huang, Meng, and

106 Ampuero (2012)): in the source domain, the element grid size is $dl = 500$ m (Figure

107 S2). Accordingly, the frequency resolution is determined by dl and the minimum wave-

108 length, that is, the minimum S wave velocity. We require at least $n = 4$ grids within

109 the minimum wavelength, so we can estimate the maximum resolvable frequency of our

110 simulations. This varies for different models. For the models with homogeneous velocity

111 structure (Models 1-3, 15-17), $V_S = 4$ km/s and the maximum frequency we can resolve is

112 $f = V_S/4dl = 2$ Hz. For the models with heterogeneous velocity structures, the maximum

113 resolvable frequency varies with minimum V_S. The minimum shear wave speed in the

114 velocity models is 0.6 km/s, corresponding to $f = min(V_S)/4dl = 0.3$ Hz. In our re-

115 sults, we will interpret radiation below this maximum frequency. We use the 2D spectral

116 element-based code SEM2DPACK (`http://www.sourceforge.net/projects/sem2d/`,

117 last accessed on 08/30/2019) to solve for the dynamic rupture. This code has been well

118 validated and applied in some previous studies (e.g., Huang & Ampuero, 2011; Huang et

119 al., 2012) to simulate the megathrust earthquakes as well as the wave fields.

In most of our simulations, we include the realistic velocity models, which have significant material contrasts in the downdip regions (Fig. 1b or Fig. S1). As proposed by (Rubin & Ampuero, 2007; Ampuero & Ben-Zion, 2008; Huang, 2018), the material contrasts can cause normal stress perturbation during dynamic rupture. They suggest to use a regularization $\dot{\sigma^*} = \frac{V^*}{D_\sigma}(\sigma - \sigma^*)$ to force the normal stress to evolve continuously. σ and σ^* are the actual normal stress and the regularized normal stress (they call it "effective" but here we use "regularized" to differentiate from the one related to pore pressure). The reference velocity V^* and slip distance D_σ are the two constitutive parameters. In our simulations, since we are focusing on the fault slip within the frequency band below 0.3 Hz, we apply a 1 s long Gaussian time window to smooth out the numerical noises in the slip rate functions. We compare models processed by different schemes and find that the slip-rate functions are almost indistinguishabl (Fig. S5).

References

Agudelo, W., Ribodetti, A., Collot, J.-Y., & Operto, S. (2009). Joint inversion of multichannel seismic reflection and wide-angle seismic data: Improved imaging and refined velocity model of the crustal structure of the north Ecuador–south Colombia convergent margin. *Journal of Geophysical Research: Solid Earth*, *114*(B2). doi: https://doi.org/10.1029/2008JB005690

Ampuero, J.-P., & Ben-Zion, Y. (2008). Cracks, pulses and macroscopic asymmetry of dynamic rupture on a bimaterial interface with velocity-weakening friction. *Geophysical Journal International*, *173*(2), 674–692. doi: 10.1111/j.1365-246X.2008.03736.x

Andrews, D. J. (1985). Dynamic plane-strain shear rupture with a slip-weakening friction law calculated by a boundary integral method. *Bulletin of the Seismological Society of America*, *75*(1), 1–21.

Bassett, D., Kopp, H., Sutherland, R., Henrys, S., Watts, A. B., Timm, C., ... Ronde, C. E. J. d. (2016). Crustal structure of the Kermadec arc from MANGO seismic refraction profiles. *Journal of Geophysical Research: Solid Earth*, *121*(10), 7514–7546. doi: https://doi.org/10.1002/2016JB013194

Bassett, D., Sutherland, R., Henrys, S., Stern, T., Scherwath, M., Benson, A., ... Henderson, M. (2010). Three-dimensional velocity structure of the northern Hikurangi margin, Raukumara, New Zealand: Implications for the growth of continental crust by subduction erosion and tectonic underplating. *Geochemistry, Geophysics, Geosystems*, *11*(10). doi: https://doi.org/10.1029/2010GC003137

Brocher, T. M. (2005). Empirical Relations between Elastic Wavespeeds and Density in the Earth's Crust. *Bulletin of the Seismological Society of America*, *95*(6), 2081–2092. doi: 10.1785/0120050077

Contreras-Reyes, E., Becerra, J., Kopp, H., Reichert, C., & Díaz-Naveas, J. (2014).

Seismic structure of the north-central Chilean convergent margin: Subduction erosion of a paleomagmatic arc. *Geophysical Research Letters*, *41*(5), 1523–1529. doi: https://doi.org/10.1002/2013GL058729

Contreras-Reyes, E., Grevemeyer, I., Flueh, E. R., & Reichert, C. (2008). Upper lithospheric structure of the subduction zone offshore of southern Arauco peninsula, Chile, at 38S. *Journal of Geophysical Research: Solid Earth*, *113*(B7). doi: https://doi.org/10.1029/2007JB005569

Contreras-Reyes, E., Grevemeyer, I., Watts, A. B., Flueh, E. R., Peirce, C., Moeller, S., & Papenberg, C. (2011). Deep seismic structure of the Tonga subduction zone: Implications for mantle hydration, tectonic erosion, and arc magmatism. *Journal of Geophysical Research: Solid Earth*, *116*(B10). doi: https://doi.org/10.1029/2011JB008434

Day, S. M. (1982). Three-dimensional simulation of spontaneous rupture: The effect of nonuniform prestress. *Bulletin of the Seismological Society of America*, *72*(6A), 1881–1902.

Dunham, E. M. (2007). Conditions governing the occurrence of supershear ruptures under slip-weakening friction. *Journal of Geophysical Research: Solid Earth*, *112*(B7). doi: 10.1029/2006JB004717

Gailler, A., Charvis, P., & Flueh, E. R. (2007). Segmentation of the Nazca and South American plates along the Ecuador subduction zone from wide angle seismic profiles. *Earth and Planetary Science Letters*, *260*(3), 444–464. doi: 10.1016/j.epsl.2007.05 .045

Graindorge, D., Calahorrano, A., Charvis, P., Collot, J.-Y., & Bethoux, N. (2004). Deep structures of the Ecuador convergent margin and the Carnegie Ridge, possible consequence on great earthquakes recurrence interval. *Geophysical Research Letters*, *31*(4). doi: https://doi.org/10.1029/2003GL018803

Hampel, A., Kukowski, N., Bialas, J., Huebscher, C., & Heinbockel, R. (2004). Ridge subduction at an erosive margin: The collision zone of the Nazca Ridge in southern Peru. *Journal of Geophysical Research: Solid Earth*, *109*(B2). doi: https://doi.org/10.1029/2003JB002593

Horning, G., Canales, J. P., Carbotte, S. M., Han, S., Carton, H., Nedimović, M. R., & Keken, P. E. v. (2016). A 2-D tomographic model of the Juan de Fuca plate from accretion at axial seamount to subduction at the Cascadia margin from an active source ocean bottom seismometer survey. *Journal of Geophysical Research: Solid Earth*, *121*(8), 5859–5879. doi: https://doi.org/10.1002/2016JB013228

Huang, Y. (2018). Earthquake Rupture in Fault Zones With Along-Strike Material Heterogeneity. *Journal of Geophysical Research: Solid Earth*, *123*(11), 9884–9898. doi: https://doi.org/10.1029/2018JB016354

Huang, Y., & Ampuero, J.-P. (2011). Pulse-like ruptures induced by low-velocity fault zones. *Journal of Geophysical Research: Solid Earth*, *116*(B12). doi: 10.1029/2011JB008684

Huang, Y., Meng, L., & Ampuero, J.-P. (2012). A dynamic model of the frequency-dependent rupture process of the 2011 Tohoku-Oki earthquake. *Earth, Planets and Space*, *64*(12), 1. doi: 10.5047/eps.2012.05.011

Hubbert, M. K., & Rubey, W. W. (1959). Role of fluid pressure in mechanics of overthrust faulting: I. mechanics of fluid-filled porous solids and its application to overthrust faulting. *GSA Bulletin*, *70*(2), 115–166. doi: 10.1130/0016-7606(1959)70[115:ROFPIM]2.0.CO;2

Klingelhoefer, F., Berthet, T., Lallemand, S., Schnurle, P., Lee, C. S., Liu, C. S., . . . Theunissen, T. (2012). P-wave velocity structure of the southern Ryukyu margin east of Taiwan: Results from the ACTS wide-angle seismic experiment. *Tectonophysics*,

578, 50–62. doi: 10.1016/j.tecto.2011.10.010

Klingelhoefer, F., Gutscher, M.-A., Ladage, S., Dessa, J.-X., Graindorge, D., Franke, D., ... Chauhan, A. (2010). Limits of the seismogenic zone in the epicentral region of the 26 December 2004 great Sumatra-Andaman earthquake: Results from seismic refraction and wide-angle reflection surveys and thermal modeling. *Journal of Geophysical Research: Solid Earth*, *115*(B1). doi: https://doi.org/10.1029/2009JB006569

Kodaira, S., Takahashi, N., Park, J.-O., Mochizuki, K., Shinohara, M., & Kimura, S. (2000). Western Nankai Trough seismogenic zone: Results from a wide-angle ocean bottom seismic survey. *Journal of Geophysical Research: Solid Earth*, *105*(B3), 5887–5905. doi: https://doi.org/10.1029/1999JB900394

Kopp, H., Weinzierl, W., Becel, A., Charvis, P., Evain, M., Flueh, E. R., ... Roux, E. (2011). Deep structure of the central Lesser Antilles Island Arc: Relevance for the formation of continental crust. *Earth and Planetary Science Letters*, *304*(1), 121–134. doi: 10.1016/j.epsl.2011.01.024

Krabbenhöft, A., Bialas, J., Kopp, H., Kukowski, N., & Hübscher, C. (2004). Crustal structure of the Peruvian continental margin from wide-angle seismic studies. *Geophysical Journal International*, *159*(2), 749–764. doi: 10.1111/j.1365-246X.2004 .02425.x

Lotto, G. C., Jeppson, T. N., & Dunham, E. M. (2018). Fully Coupled Simulations of Megathrust Earthquakes and Tsunamis in the Japan Trench, Nankai Trough, and Cascadia Subduction Zone. *Pure and Applied Geophysics*. doi: 10.1007/s00024-018 -1990-y

Martínez-Loriente, S., Sallarès, V., Ranero, C. R., Ruh, J. B., Barckhausen, U., Grevemeyer, I., & Bangs, N. (2019). Influence of Incoming Plate Relief on Overriding Plate Deformation and Earthquake Nucleation: Cocos Ridge Subduction (Costa Rica).

Tectonics, *38*(12), 4360–4377. doi: https://doi.org/10.1029/2019TC005586

Miura, S., Suyehiro, K., Shinohara, M., Takahashi, N., Araki, E., & Taira, A. (2004). Seismological structure and implications of collision between the Ontong Java Plateau and Solomon Island Arc from ocean bottom seismometer–airgun data. *Tectonophysics*, *389*(3), 191–220. doi: 10.1016/j.tecto.2003.09.029

Miura, S., Takahashi, N., Nakanishi, A., Tsuru, T., Kodaira, S., & Kaneda, Y. (2005). Structural characteristics off Miyagi forearc region, the Japan Trench seismogenic zone, deduced from a wide-angle reflection and refraction study. *Tectonophysics*, *407*(3), 165–188. doi: 10.1016/j.tecto.2005.08.001

Moscoso, E., Grevemeyer, I., Contreras-Reyes, E., Flueh, E. R., Dzierma, Y., Rabbel, W., & Thorwart, M. (2011). Revealing the deep structure and rupture plane of the 2010 Maule, Chile earthquake (Mw=8.8) using wide angle seismic data. *Earth and Planetary Science Letters*, *307*(1), 147–155. doi: 10.1016/j.epsl.2011.04.025

Murphy, S., Di Toro, G., Romano, F., Scala, A., Lorito, S., Spagnuolo, E., . . . Nielsen, S. (2018). Tsunamigenic earthquake simulations using experimentally derived friction laws. *Earth and Planetary Science Letters*, *486*, 155–165. doi: 10.1016/j.epsl.2018.01.011

Nakanishi, A., Kurashimo, E., Tatsumi, Y., Yamaguchi, H., Miura, S., Kodaira, S., . . . Hirata, N. (2009). Crustal evolution of the southwestern Kuril Arc, Hokkaido Japan, deduced from seismic velocity and geochemical structure. *Tectonophysics*, *472*(1), 105–123. doi: 10.1016/j.tecto.2008.03.003

Nakanishi, A., Takahashi, N., Park, J.-O., Miura, S., Kodaira, S., Kaneda, Y., . . . Nakamura, M. (2002). Crustal structure across the coseismic rupture zone of the 1944 Tonankai earthquake, the central Nankai Trough seismogenic zone. *Journal of Geophysical Research: Solid Earth*, *107*(B1), EPM 2–1–EPM 2–21. doi:

256   https://doi.org/10.1029/2001JB000424

257 Nishizawa, A., Kaneda, K., Oikawa, M., Horiuchi, D., Fujioka, Y., & Okada, C. (2017).

258   Variations in seismic velocity distribution along the Ryukyu (Nansei-Shoto) Trench

259   subduction zone at the northwestern end of the Philippine Sea plate. *Earth, Planets*

260   *and Space*, *69*(1), 86. doi: 10.1186/s40623-017-0674-7

261 Planert, L., Kopp, H., Lueschen, E., Mueller, C., Flueh, E. R., Shulgin, A., . . . Krabben-

262   hoeft, A. (2010). Lower plate structure and upper plate deformational segmentation

263   at the Sunda-Banda arc transition, Indonesia. *Journal of Geophysical Research: Solid*

264   *Earth*, *115*(B8). doi: https://doi.org/10.1029/2009JB006713

265 Rice, J. R. (1992). Chapter 20 Fault Stress States, Pore Pressure Distributions, and the

266   Weakness of the San Andreas Fault. In B. Evans & T.-f. Wong (Eds.), *International*

267   *Geophysics* (Vol. 51, pp. 475–503). Academic Press. doi: 10.1016/S0074-6142(08)

268   62835-1

269 Rubin, A. M., & Ampuero, J.-P. (2007). Aftershock asymmetry on a bimaterial interface.

270   *Journal of Geophysical Research: Solid Earth*, *112*(B5). doi: https://doi.org/10

271   .1029/2006JB004337

272 Sallarès, V., Dañobeitia, J. J., & Flueh, E. R. (2001). Lithospheric structure of the

273   Costa Rican Isthmus: Effects of subduction zone magmatism on an oceanic plateau.

274   *Journal of Geophysical Research: Solid Earth*, *106*(B1), 621–643. doi: https://

275   doi.org/10.1029/2000JB900245

276 Scherwath, M., Contreras-Reyes, E., Flueh, E. R., Grevemeyer, I., Krabbenhoeft, A.,

277   Papenberg, C., . . . Weinrebe, R. W. (2009). Deep lithospheric structures along

278   the southern central Chile margin from wide-angle P-wave modelling. *Geophysical*

279   *Journal International*, *179*(1), 579–600. doi: 10.1111/j.1365-246X.2009.04298.x

280 Shulgin, A., Kopp, H., Mueller, C., Planert, L., Lueschen, E., Flueh, E. R., & Djajadi-

hardja, Y. (2011). Structural architecture of oceanic plateau subduction offshore Eastern Java and the potential implications for geohazards. *Geophysical Journal International*, *184*(1), 12–28. doi: 10.1111/j.1365-246X.2010.04834.x

Takahashi, N., Suyehiro, K., & Shinohara, M. (1998). Implications from the seismic crustal structure of the northern Izu–Bonin arc. *Island Arc*, *7*(3), 383–394. doi: https://doi.org/10.1111/j.1440-1738.1998.00197.x

Walther, C. H. E., Flueh, E. R., Ranero, C. R., Von Huene, R., & Strauch, W. (2000). Crustal structure across the Pacific margin of Nicaragua:evidence for ophiolitic basement and a shallow mantle sliver. *Geophysical Journal International*, *141*(3), 759–777. doi: 10.1046/j.1365-246x.2000.00134.x

Ye, S., Flueh, E. R., Klaeschen, D., & von Huene, R. (1997). Crustal structure along the EDGE transect beneath the Kodiak shelf off Alaska derived from OBH seismic refraction data. *Geophysical Journal International*, *130*(2), 283–302. doi: 10.1111/ j.1365-246X.1997.tb05648.x

Zhu, J., Kopp, H., Flueh, E. R., Klaeschen, D., Papenberg, C., & Planert, L. (2009). Crustal structure of the central Costa Rica subduction zone: Implications for basal erosion from seismic wide-angle data. *Geophysical Journal International*, *178*(2), 1112–1131. doi: 10.1111/j.1365-246X.2009.04208.x
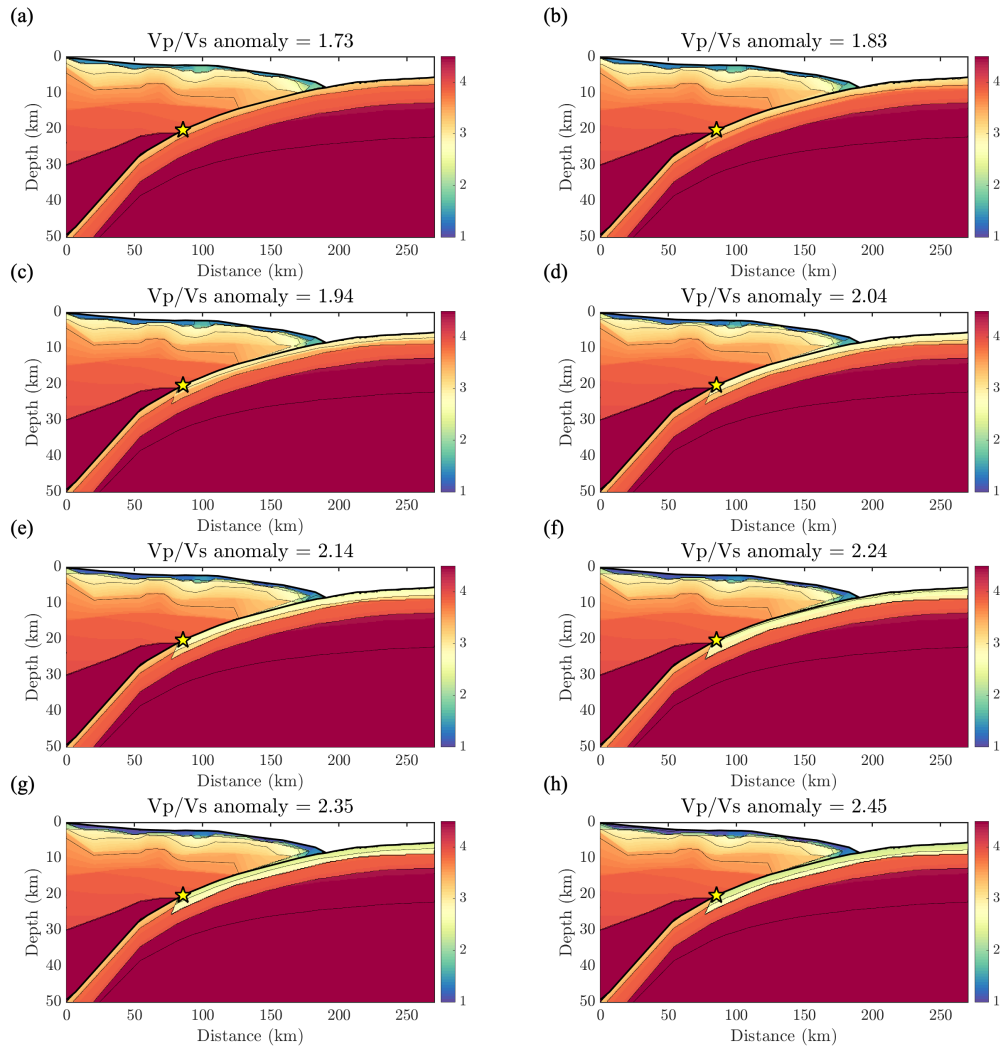
Figure S1. Corresponding S wave velocity from different settings of Vp/Vs ratios: (a) Vp/Vs = 1.73; (b) Vp/Vs = 1.84; (c) Vp/Vs = 1.94; (d) Vp/Vs = 2.04; (e) Vp/Vs = 2.14; (f) Vp/Vs = 2.24; (g) Vp/Vs = 2.34; (h) Vp/Vs = 2.45.
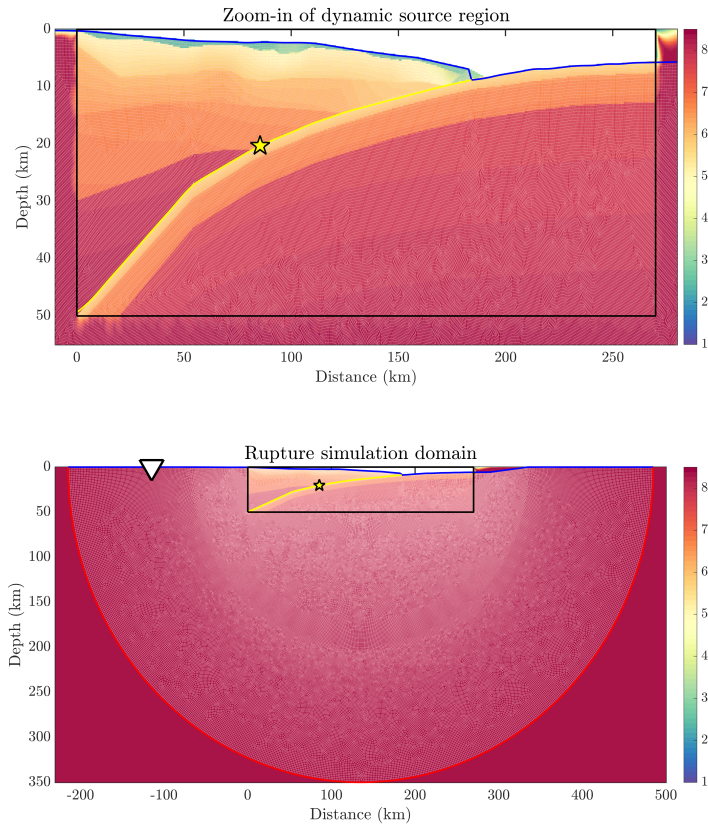
Figure S2. **Domain of dynamic simulations**. (top) The near-source region with various model settings. Blue and yellow lines indicate the free surface and dynamic fault, respectively. The color image shows the P wave velocity from Miura et al. (2005). The star indicates the hypocenter of simulated megathrust earthquakes. (bottom) Entire simulation domain. The red semicircle indicates the domain boundary with absorbing conditions. The unstructured mesh is shown in white on top of the simulation domain.

(a)

(b)
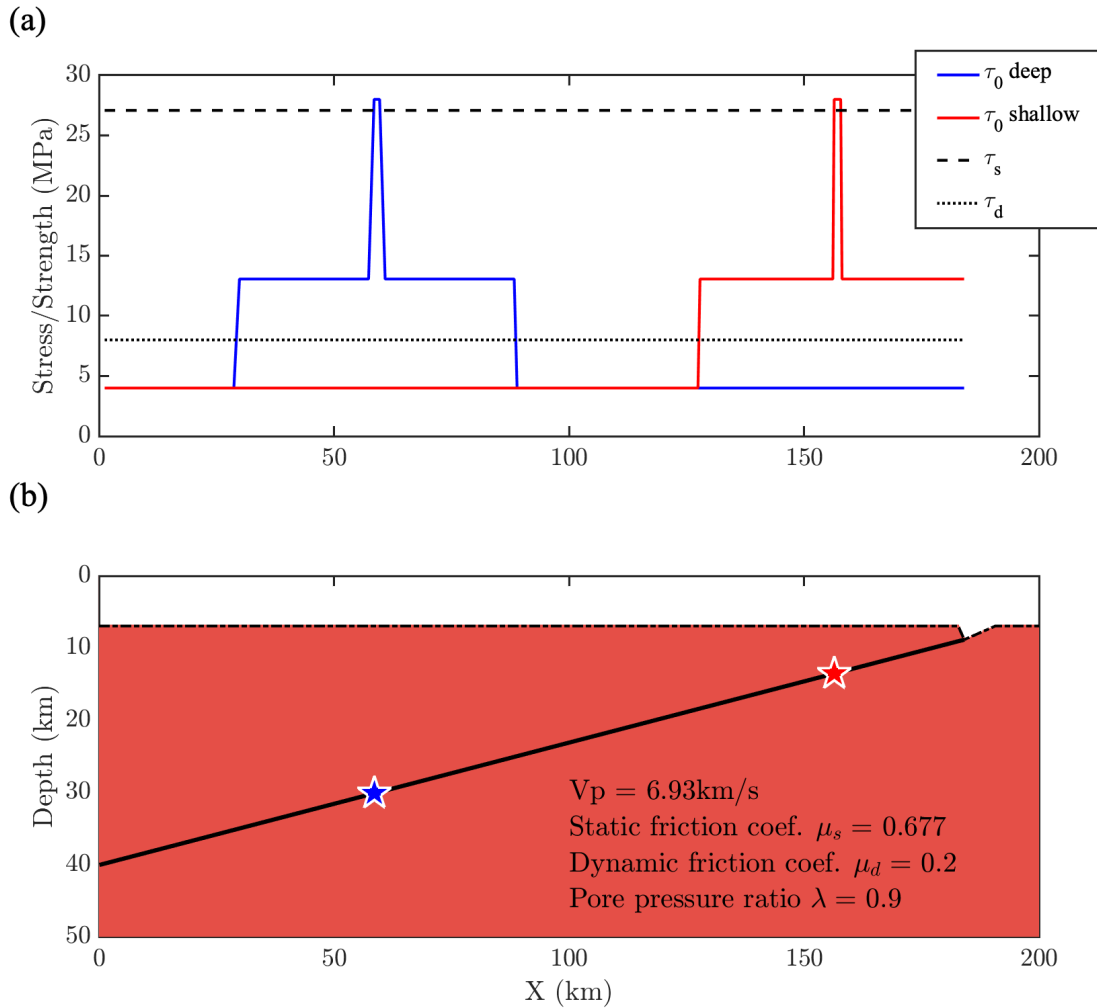
Figure S3. **Model settings of the two small rupture models**. (a) Stress/strength distribution along slab (in X coordinate): the black dot line and dashed line show the dynamic friction τ_d and static friction τ_s, respectively. Red and blue lines indicate the initial shear stress τ_0 distributions of shallow and deep earthquakes, respectively. (b) Homogeneous simulation domain with planar slab geometry and flat topography for the two small rupture models. The red and blue star indicate the location of nucleation/hypocenters of shallow and deep earthquakes, respectively.

(a) Individual points

(b) 10-km fault segments

(c)

Legend:
- Homogeneous, planar, flat, $\lambda = 0.9$
- Homogeneous, curved, flat, $\lambda = 0.9$
- Homogeneous, curved, real, $\lambda = 0.9$
- Shallow friction neutral, $\lambda = 0.9$
- Shallow friction hardening, $\lambda = 0.9$
- Exponential SW, $\lambda = 0.9$
- Vp/Vs = 1.73, $\lambda = 0.9$
- Vp/Vs = 1.83, $\lambda = 0.9$
- Vp/Vs = 1.94, $\lambda = 0.9$
- Vp/Vs = 2.04, $\lambda = 0.9$
- Vp/Vs = 2.14, $\lambda = 0.9$
- Vp/Vs = 2.24, $\lambda = 0.9$
- Vp/Vs = 2.35, $\lambda = 0.9$
- Vp/Vs = 2.45, $\lambda = 0.9$
- Homogeneous model median
- All model median
- Homogeneous, planar, flat, $\lambda = 0.7$
- Homogeneous, curved, flat, $\lambda = 0.7$
- Homogeneous, curved, real, $\lambda = 0.7$
- Shallow friction neutral, $\lambda = 0.7$
- Shallow friction hardening, $\lambda = 0.7$
- Exponential SW, $\lambda = 0.7$
- Vp/Vs = 1.73, $\lambda = 0.7$
- Vp/Vs = 1.83, $\lambda = 0.7$
- Vp/Vs = 1.94, $\lambda = 0.7$
- Vp/Vs = 2.04, $\lambda = 0.7$
- Vp/Vs = 2.14, $\lambda = 0.7$
- Vp/Vs = 2.24, $\lambda = 0.7$
- Vp/Vs = 2.35, $\lambda = 0.7$
- Vp/Vs = 2.45, $\lambda = 0.7$
- Heterogeneous model median
- Fullspace, curved, $\lambda = 0.9$

Figure S4. Spectral parameter fitting results: corner frequency f_c variation along slab from (a) individual points and (b) from fault segment averaged slip rate functions. (c) Spectral falloff rate n variation along slab. Same symbols are used as the Figure 3 in the main text.
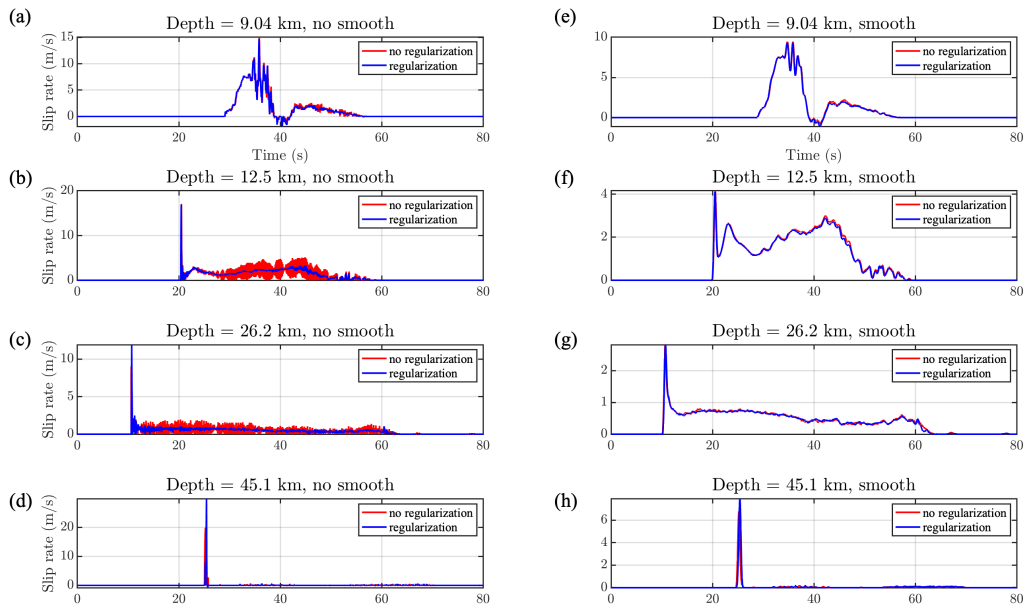
Figure S5. Comparisons of slip rate with different processing at different depths at 9.04 km, 12.5 km, 26.2 km and 45.1 km: (a) - (d) slip-rate functions from the model with (blue) and without (red) normal stress regularization; (e) - (h) slip-rate functions from the model with (blue) and without (red) normal stress regularization after the Gaussian time window smoothing.

February 10, 2021, 5:06pm

Table S1. Range in V$_P$ values in the downgoing slab low velocity zone LVZ (V_{LVZ}) and in

the overhanging continental crust (V_{cont}) for various subduction zones.

Subduction zone	Reference	V_{LVZ} (km/s)	V_{cont} (km/s)
Alaska	Ye, Flueh, Klaeschen, and von Huene (1997)	4.9 - 5.1	4.6 - 5.1
Antilles	Kopp et al. (2011)	5.5 - 6.0	6.5 - 8.0
Cascadia	Horning et al. (2016)	4.0 - 4.5	4.5 - 6.5
Chile 1	Contreras-Reyes, Grevemeyer, Flueh, and Reichert (2008)	3.5 - 4.8	5.5 - 6.0
Chile 2	Scherwath et al. (2009)	4.5 - 5.0	5.0 - 7.0
Chile 3	Moscoso et al. (2011)	4.5 - 6.0	6.0 - 6.9
Chile 4	Contreras-Reyes, Becerra, Kopp, Reichert, and Díaz-Naveas (2014)	4.0 - 5.0	5.5 - 7.0
Costa Rica 1	Walther, Flueh, Ranero, Von Huene, and Strauch (2000)	5.5 - 6.0	5.7 - 8.3
Costa Rica 2	Sallarès, Dañobeitia, and Flueh (2001)	5.0 - 6.3	5.9 - 7.2
Costa Rica 3	Zhu et al. (2009)	3.0 - 4.0	4.5 - 6.0
Costa Rica 4	Martínez-Loriente et al. (2019)	4.0 - 5.0	4.0 - 6.5
Ecuador 1	Graindorge, Calahorrano, Charvis, Collot, and Bethoux (2004)	5.0 - 6.0	6.0 - 6.7
Ecuador 2	Gailler, Charvis, and Flueh (2007)	4.5 - 6.0	4.5 - 6.5
Ecuador 3	Agudelo, Ribodetti, Collot, and Operto (2009)	4.5 - 6.0	6.0 - 7.0
Izu Bonin	Takahashi, Suyehiro, and Shinohara (1998)	4.7 - 6.4	5.7 - 7.4
Java 1	Planert et al. (2010)	3.0 - 4.5	5.0 - 7.6
Java 2	Shulgin et al. (2011)	5.0 - 6.0	5.0 - 7.5
Kuril	Nakanishi et al. (2009)	4.5 - 6.0	6.0 - 8.0
Nankai Trough 1	Kodaira et al. (2000)	5.2 - 5.8	5.2 - 6.7
Nankai Trough 2	Nakanishi et al. (2002)	4.2 - 5.4	5.0 - 6.8
New Zealand	Bassett et al. (2010)	4.9 - 6.3	6.8 - 8.5
Nicaragua 1	Walther et al. (2000)	5.5 - 6.9	5.9 - 8.3
Peru 1	Hampel, Kukowski, Bialas, Huebscher, and Heinbockel (2004)	4.5 - 5.0	4.2 - 5.5
Peru 2	Krabbenhöft, Bialas, Kopp, Kukowski, and Hübscher (2004)	4.0 - 6.1	5.7 - 6.5
Ryukyu	Nishizawa et al. (2017)	5.0 - 6.0	5.0 - 7.0
Sumatra	Klingelhoefer et al. (2010)	5.0 - 6.0	5.0 - 8.0
Solomon	Miura et al. (2004)	5.0 - 6.3	5.3 - 6.9
Taiwan	Klingelhoefer et al. (2012)	5.5 - 6.0	4.5 - 7.0
Tohoku	Miura et al. (2005)	5.5 - 6.6	5.5 - 8.0
Tonga 1	Contreras-Reyes et al. (2011)	5.5 - 6.5	6.0 - 7.5
Tonga 2	Bassett et al. (2016)	3.8 - 4.5	4.5 - 7.9